SUPPLEMENTAL MATERIAL

Dynamically manipulating topological physics and edge modes in a single degenerate optical cavity

Xiang-Fa Zhou, Xi-Wang Luo, Su Wang, Guang-Can Guo, Xingxiang Zhou, Han Pu, Zheng-Wei Zhou

In this Supplemental Material, we provide some basic background about degenerated cavity where technique details inside the ancillary circuits are clarified to implement the desired hoppings. The reduction of hopping amplitudes due to the size effect of pinhole in each beam splitter is also discussed. The calculation details about Floquet topological system are also provided.

I. DEGENERATED CAVITY AND EFFECTIVE CONSTRUCTION OF 1D LATTICE WITH BOUNDARIES

For a ring-type cavity which is made of optical elements with cylindrical symmetry, the cavity mode are the Laguerre-Gaussian (LG) modes $E_{p,l}$, with p, l the radial and azimuthal index respectively. Its resonance frequency is determined by

$$kL_0 - (2p + l + 1)\arccos\frac{A+D}{2} = 2n\pi, \tag{S1}$$

where L_0 is the length of the round-trip optical path, and A and D are diagonal elements in the round-trip ray matrix. The off-diagonal elements of the round-trip ray matrix, B and C, only affect the beam waist of the resonance modes. n is an integer. If we design the cavity such that $A = D = 1$ and $B = C = 0$, then the resonance frequency becomes independent of p and l, and such a cavity is called a degenerate cavity [s33, 35]. It can support photon modes of different p and l simultaneously. The LG mode $E_{l,p}$ carries an OAM of $l\hbar$ per photon, thus the degenerate cavity could support photon modes in different OAM states. Our simulator are shown in Fig. s1, and the optical designs are:

1. The length of the main cavity is chosen for constructive interference, $kL_0 = 2n\pi$. The elements of the ray matrix for the optical paths $BS_1 \to BS_2$ and $BS_2 \to BS_1$ in the main cavity are $A = D = -1$, $B = C = 0$.

2. The auxiliary cavity consisting of the two beam splitters BS_1, BS_2 and the two spatial light modulators SLM_1, SLM_2. Its length is chosen for destructive interference, $kL_0 = (2n + 1)\pi$. The elements of the ray matrix for optical paths $SLM_1 \to BS_2 \to SLM_2$ and $SLM_2 \to BS_1 \to SLM_1$ are $A = D = -1$, $B = C = 0$.

Such a simulator is conceptually equivalent to a 1D lattice, with the lattice sites represented by the OAM states (See Fig. s1). The SLMs change the OAM of light by $\delta_l = \pm 1$ depending on the incident direction. The BSs split a portion of the light in the main cavity to the SLMs and merge it back, this corresponds to photon tunneling between neighbor lattice sites. In addition, long-range tunneling could be realized by a separate auxiliary cavity consisting SLMs that change the OAM of photon by $\pm m$ with $m > 1$. The Hamiltonian of the system reads

$$\mathcal{H} = -\kappa\sum_l \left(e^{i\phi}\hat{a}_{l+1}^\dagger \hat{a}_l + h.c.\right), \tag{S2}$$

where the tunneling strength is $\kappa = \Omega_0|r|^2/4\pi$ with r the reflectivity coefficient and Ω_0 the free spectral range of the main cavity. The tunneling phase ϕ is determined by the phase imbalance between the two arms of the auxiliary cavity, it could be either OAM independent or OAM dependent. A beam rotator, consisting of two Dove prisms which are rotated by $\theta/2$ with respect to each other, will rotate the beam by an angle of θ, based on which, we obtain an OAM dependent phase $e^{il\theta}$ to the light beam, as shown in Fig. s1. Putting a beam rotator with rotating angle $\pm\theta$ in each arm of the auxiliary cavity, we obtain a OAM dependent tunneling phase $\phi = \phi_0 + l\theta_0$, with ϕ_0 the phase imbalance caused by the optical path length.

The tunneling coefficient could be tuned by an interference mechanism. If we introduce another auxiliary cavity with tunneling phase $\phi = \phi_1 + l\theta_1$, then the tunneling coefficient would become $\kappa[e^{i(\phi_0+l\theta_0)} + e^{i(\phi_1+l\theta_1)}]$. In particular, if $\phi_0 = -\phi_1$ and $\theta_0 = -\theta_1$, the tunneling coefficient becomes $\kappa\cos(\phi_0 + l\theta_0)$.

When the beam sizes is comparable with the cavity mirror, leakage of photons outside the cavity is unavoid-

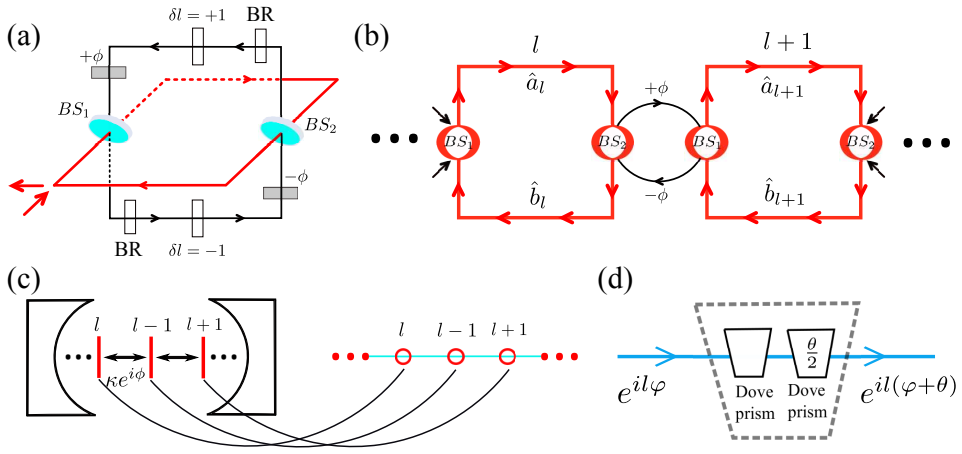

FIG. s1: (Color online). (a) Illusion of experiment setup about the degenerate cavity of our simulator. (b) is the effective photonic circuit of (a). ϕ is the imbalanced phase between the two arms of the auxiliary cavity. (c) Mapping of the simulator to a 1D lattice. BR is beam rotator that rotates the light beam by an angle of θ as shown in (d). It introduces a OAM-dependent phase to the beam $e^{il\varphi} \to e^{il(\varphi+\theta)}$.

able due to the typical intensity distributions of LG modes. For instance, the intensity profile of $E_l^{p=0}$ mode reaches its maximal when $r = \sqrt{l/2}$. We stress that for $p \neq 0$, the mode becomes more spatially extended along the radial direction. In experiments, the cavity modes can be excited by feeding the cavity with Gaussian beams E_0^0 such that the waists of the beams overlap with the SLMs. Using this setting, all high order modes with $p > 0$ can be greatly suppressed. When $l \gg 1$, two adjacent OAM modes E_l^0 and E_{l+1}^0 becomes almost completely overlap with each other, which makes it extremely difficult to distinguish them from their intensity distributions. In addition, if we consider a finite radius $\sqrt{L/2}$ of cavity mirrors, the portion of photons $P(l) = \int_{\sqrt{L/2}}^{\infty} dr r |E_l^0|^2$ outside the radius increases almost exponentially as $l \to L$ (see Fig. s2). This leads to the fast increasement of decay rate for cavity modes near the nature boundaries of the effective lattice. For topological nontrivial system, these factors result in serious photonic loss which can annihilate almost all interesting phenomena related to edge physics (see Fig. 4 in the paper).

To construct an effective boundaries of the 1D chain, we make use of the fact that only the zero OAM mode has a high intensity at the beam center, in contrast with doughnut beam shapes for $l \neq 0$ modes. We make proper design of the optical circuit so that we select $l = 0$ as boundary by spatial filtering. This is achieved by introducing composite structure of the cavity modes with the help of hollow BSs and SLMs. The explicit construction is depicted in Fig. 2. Specifically, if we start with a composite mode $[0, -L_m]$ inside the main cavity, this modified auxiliary cavity can only induce an effective hopping between modes $[0, -L_m] \to [1, -L_m + 1]$, where photons can only be reflected into the auxiliary circuit through BS_2 on the right arm in the main cavity. The SLMs with

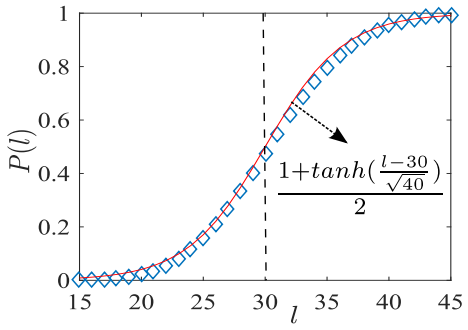

FIG. s2: (Color online). The portion $P(l)$ of photons outside the cavity with fixed mirror size $r = \sqrt{30/2}$, which increases exponentially as $l \to 30$. The data is fitted by the red solid line.

$\delta l = \pm(L_m+1)$ in the auxiliary circuit induces a photonic OAM changing from $l = -L_m+1$ to $l = 1$, which ensures that photons can then be diverted back to the main cavity through BS_1 and overlap with the modes $[1, -L_m+1]$. We note that the tunneling $[0, L_m] \leftrightarrow [-1, -L_m - 1]$ is blocked since a hollow BS_1 on the left arm cannot reflect photons with $l = 0$ into the auxiliary circuits. Similar discussion also applies to the mode $[L_m, 0]$. Therefore, using this special setting, one can realize an effective finite hopping chain as $[0, -L_m] \leftrightarrow [1, -L_m+1] \cdots [L_m, 0]$ with $[0, -L_m]$ and $[L_m, 0]$ acting as the effective boundaries.

As an example, in the main text, we have shown the explicit construction of a finite SSH chain based on the above design, where two different ancillary circuits are introduced to implement the corresponding two hopping terms shown in Eq. (1). Here for given OAM l of photon mode E_l, we map it to two different lattice sites labeled as $2l$ and $2l + 1$ by taking into account their inner polarization degrees of freedom $a_{2l} \to E_{l,H}$ and

$a_{2l+1} \rightarrow E_{l,V}$ with H and V corresponding to the horizontal and vertical polarized states respectively. The hopping $a^{\dagger}_{2l}a_{2l+1} + h.c.$ involves only cavity modes with the same OAM l and different polarizations, which can be implemented by introducing spin-flip operator inside the auxiliary cavity, as shown in Fig.'(3b) in the main text. Since the upper and lower arms in the auxiliary cavity depicted in Fig. 3(b) provide two different polarization flip channels with opposite phase retardation, the interference of the two arms results in a phase dependent coupling proportional to $\cos\phi$, and as a result the phase delay ϕ becomes a convenient control knob to adjust the hopping amplitude $J_0' \equiv J_0 \cos\phi$.

The hopping Hamiltonian $a^{\dagger}_{2l+1}a_{2l+2}+h.c.$ corresponds to the coupling of optical modes $E_{l,V} \leftrightarrow E_{l+1,H}$, which becomes polarization-dependent as only OAM of vertical (horizontal) polarized modes can be increased (decreased) through the ancillary circuit. To implement such polarization-dependent OAM hopping $l \rightarrow l+1$, we introduce two additional optical circuits for horizontal polarized modes with the help of polarized beam-splitters (PBS) (See Fig. 3c). The PBSs are designed such that only vertical polarized photons can go through while horizontal polarized beams are reflected. One can see that for an incoming optical mode E_{l-Lm} from the right BS, only vertical polarized mode $E_{l-L_m,V}$ can pass through the SLM at the top of the circuit, which realizes the hopping $E_{l-L_m,V} \rightarrow E_{l+1,V}$. The polarization of this mode is then flipped by inserting a HWP before it reaches the left BS and couples back into the main circuit. We note that the horizontal mode $E_{l-L_m,H}$ has been reflected back to the right BS by PBSs to hinder the unwanted hopping $E_{l-L_m,H} \rightarrow E_{l+1,H}$. Using these setting, we have succeed in implementing the desired polarization-dependent hopping $E_{l-L_m,V} \rightarrow E_{l+1,H}$. Similar discussion also works for the hopping $E_{l+1,H} \rightarrow E_{l-L_m,V}$ with incoming mode $E_{l+1,H}$ from the left BS shown in Fig. 3c. This combined circuit thus realizes the expected hopping Hamiltonian we outlined above.

II. EFFECTIVE HOPPING AND DECAY DUE TO THE PRESENCE OF PINHOLE IN THE BEAM SPLITTERS

The presence of pinhole in each beam splitter in this modified cavity circuits distorts the optical modes , which may result in the reduction of effective hopping amplitudes κ and other unwanted decay of these modes. To estimate the influence of the holes, we need to know the explicit distributions of these optical modes inside the cavity. Under the paraxial approximation, the electric fields at two planes (x_0, y_0, z_0) and (x_1, y_1, z_1) can be connected through the Collins integral defined as [s36]

$$e^{-ikz_1}E_1(x_1,y_1) = e^{-ikL}e^{-ikz_0}\frac{i}{\lambda B}\int\int dx_0 dy_0 E_0(x_0,y_0) * \exp\{-\frac{i}{\lambda B}[A(x_0^2+y_0^2)+D(x_1^2+y_1^2)-2(x_0x_1+y_0y_1)], \tag{S3}$$

where λ and k are the wavelength and wave number of the beams, and L is the length of the optical path between the two planes with the ray transfer matrix defined by $M = \begin{bmatrix} A & B \\ C & D \end{bmatrix}$ [s37]. Therefore, starting with the Gaussian mode with $l = 0$, if we excite the cavity modes such that the beam waists overlap with the SLMs, other cavity modes after passing the SLMs can be obtained by imposing different factors $e^{-il\theta}$ on these beams with different orbital angular momentum l. The electric fields at the BSs for different l can then be estimated by the above integral using the transfer matrix $M = \begin{bmatrix} 0 & f \\ -1/f & 0 \end{bmatrix}$ with f the focal length of cavity mirrors.

Figure 2(b) of the main text shows the calculated optical intensity profiles on the BSs for different l. One can see that the $l = 0$ mode can be easily distinguished from other modes with $l \neq 0$. To obtain an effective sharp boundary, the hole size is designed such that most portion of $l = 0$ mode can go through while most $l = 1$ mode is reflected by BSs into the ancillary cavity. This is achieved if we choose the radius r_h of the hole such that $\int_0^{r_h} drr|E_{l=0}|^2 = \int_{r_h}^{\infty} drr|E_{l=1}|^2$, where E_l are the electric fields on the BSs obtained from Eq. S3. For instance, if we choose a large hopping step in the ancillary circuit with $\delta l = \pm(L_m + n)$, then we have $\int_0^{r_h} drr|E_{l=0}|^2 = \int_{r_h}^{\infty} drr|E_{l=n}|^2$. In this case, the logical lattice site j is represented by the composite mode $|l = jn\rangle$. The influence of the hole on the optical modes E_n can be estimated from

$$\begin{aligned} \eta_1^{(n)} = \int_0^{r_h} drr|E_n|^2 &\leq |E_0(r_h)|^{-2}\int_0^{r_h} drr|E_n|^2|E_0|^2 \\ &\leq |E_0(r_h)|^{-2}\int_0^{\infty} drr|E_n|^2|E_0|^2, \end{aligned} \tag{S4}$$

which scales as $\eta_1^{(n)} \sim e^{-n}$ for the usual LG mode $E_l^{p=0}$, and is consistent with our numerical calculation, as shown in Fig. s3. Therefore, a larger hopping step is always helpful for the construction of sharp boundaries.

The reflection of $|l = 0\rangle$ mode at the BSs leads to the coupling of the composite modes $|0\rangle$ and $|-n\rangle$, which may soften the boundary we have designed. This amplitude can be estimated as $\eta_1^{(n)}\kappa$, as $\eta_1^{(n)}$ describes the portion of photon that has been reflected into the ancillary cavity at BS1 to realize the unwanted hopping $|0\rangle \rightarrow |l = -n\rangle$. Meanwhile, the effective coupling between modes $|0\rangle$ and $|n\rangle$ is also weakened, which can be estimated by $(1 -$

n	1	2	3	4	5
$r_h(mm)$	0.123	0.154	0.180	0.204	0.224
$\eta_1^{(n)}$	0.22	0.095	0.039	0.017	0.007

TABLE sI: Calculated radius r_h of the pinhole in the beam splitter and the factor $\eta_1^{(n)}$ for different hopping step n. Here we choose the cavity mirrors' focal length $f = 10cm$, and the wavenumber $\lambda = 0.885 \times 10^{-3}mm$. The Gaussian beam for the $l = 0$ mode at the SLM is $E_{l=0} = E_0 e^{-r^2/w_0^2}$ with the waist size $w_0 = 0.2mm$.

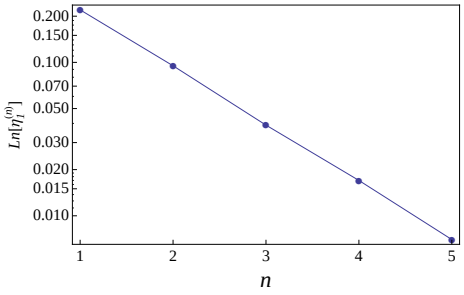

FIG. s3: (Color online). Calculated $\eta_1^{(n)}$ for different hopping step n, which scales exponentially along with n.

$\eta_1^{(n)})\kappa$ since part of the $|l = n\rangle$ modes in the ancillary cavity cannot couple back into the main cavity due to the presence of the pinhole. Similar discussion also applies to other cavity modes $|l = jn\rangle$, where effective coupling between modes $|(j-1)n\rangle$ and $|jn\rangle$ has been reduced to $(1 - \eta_j^{(n)})\kappa$ with $\eta_j^{(n)}$ defined as $\eta_j^{(n)} = \int_0^{r_h} drr|E_{jn}|^2$. The calculation shows that $\eta_j^{(n)}$ also scales exponentially along with the lattice site j, as shown in Tab. sII and Fig. s5. This indicates that only the logically adjacent modes with $|l = 0\rangle$, and $|l = \pm n\rangle$ are significantly affected due to the presence of the pinhole in the BSs.

j	1	2	3	4
$\eta_j^{(1)}$	0.22	0.036	0.004	3.0×10^{-4}
$\eta_j^{(2)}$	0.095	0.002	2.2×10^{-5}	1.2×10^{-7}
$\eta_j^{(3)}$	0.039	1.3×10^{-4}	1.2×10^{-7}	0

TABLE sII: Calculated $\eta_j^{(n)}$ along with the lattice site j for different hopping steps $n = 1,\ 2\ ,$ and 3 respectively. Other parameters for cavities are the same with those in table sI. These parameters have also been token into account during the calculation of results shown in Fig. 4 in the main context.

Based on the above discussion, the total Hamiltonian of the 1D chain we simulated in Fig. 3 can then be written as

$$H_T = H + H' \tag{S5}$$

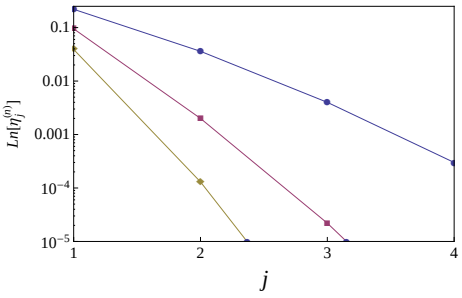

FIG. s4: (Color online). Log plots of $\eta_j^{(n)}$ along with the lattice site j for different hopping steps $n = 1,\ 2\ ,$ and 3 respectively, which scales exponentially along with j.

with

$$\begin{aligned} H &= \sum_{l=0}^{L_m} \left[J_0 \cos(\phi) a_{2l}^\dagger a_{2l+1} + J_1 \alpha_{l+1}^{(n)} a_{2l+1}^\dagger a_{2l+2} + h.c.\right] \\ H' &= H_L + H_{L0} + H_{R0} + H_R. \end{aligned}$$

Here due to the construction, the system has been divided into three pieces: H is the Hamiltonian of the center piece which we focus on, and takes the exact form of the celebrated SSH model Hamiltonian in the idea case when $\alpha_{l+1}^{(n)} = 1$; H_L and H_R represent the Hamiltonian of the left and right subchains and read

$$\begin{aligned} H_L &= \sum_{l=L_{max}}^{-1} \left[J_1 \alpha_l^{(n)} a_{2l-1}^\dagger a_{2l} + J_0 \cos(\phi) a_{2l}^\dagger a_{2l+1} + h.c.\right] \\ H_L &= \sum_{l=L_m+1}^{L_{max}} \left[J_0 \cos(\phi) a_{2l}^\dagger a_{2l+1} + J_1 \alpha_{l+1}^{(n)} a_{2l+1}^\dagger a_{2l+2} + h.c.\right] \end{aligned}$$

with L_{max} the maximal allowed OAM of photonic modes inside the cavity. Finally, the size effect of the pinhole in BSs also induces an additional coupling between H and $H_{L(R)}$ denoted by

$$\begin{aligned} H_{L0} &= \eta_1^{(n)} J_1 (a_{-1}^\dagger a_0 + h.c.) \\ H_{R0} &= \eta_1^{(n)} J_1 (a_{2L_m+1}^\dagger a_{2L_m+2} + h.c.) \end{aligned}$$

In the ideal case $\eta_1^{(n)} = 0$, the three pieces are totally disconnected. Therefore, we arrive an exact SSH model Hamiltonian as we desire. The presence of finite $\eta_1^{(n)}$ induces weak coupling between the center chain and the bilateral chains, which may soften the boundary effect of the center chain as the edge modes can tunnel into the other two sublattices. Especially, in the topological nontrivial regime, edge zero-modes appear at the ends of each subchain. In this case, H_{L0} and H_{R0} induce in effective coupling of these edge modes around each end of the center subchain. This may result in the recombination of the wavefunctions of edge modes and induce a finite energy shift around $\omega = 0$.

In Fig. 4, we have calculated the transmission rate $\tau(\omega)$ for hopping step $n = 2$ using parameters we list

above. The calculation shows that in topological nontrivial regime with $J_0'/J_1 < 1$, $\tau(\omega)$ exhibits two different branches around $\omega = 0$ with finite energy splitting. This clearly demonstrates the modification of edge modes due to the presence of weak coupling $H_{L(R)}$ at the ends of the center sublattice. For larger hopping step $n = 4$, the splitting of the two branches becomes indistinguishable due to the fast decreasement of $\eta_1^{(n)}$ along with n. In this case, we can only focus on the center subchain, while the influence of the bilateral sublattices can be neglected.

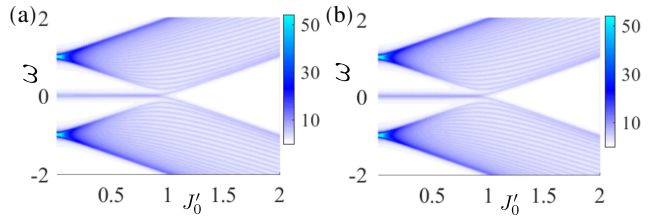

FIG. s5: (Color online). (a) and (b) show the calculated transmission rates $\tau(\omega)$ for a prolonged 1D chain with Hamiltonian S5 and a simplified Hamiltonian H in Eq. (1) respectively. The two models almost provide the same $\tau(\omega)$. Other parameters are the same with those in Fig. 4 in the main text.

We have also calculated $\tau(\omega)$ for 1D chain with soft boundaries. In this case, the presence of edge modes is completely erased, which clearly shows the necessity of boundary construction for observing topological edge modes. Finally, the dynamical properties of edge modes for different hopping steps n are also studied, as shown in Fig. 4(d) and 4(e). When $n = 1$, $N_0(t = 15)$ exhibits an oscillation along with J_0'. This is due to the interference effect of the two modified edge modes around $\omega = 0$ in the presence of finite $\eta_1^{(n)}$. For larger hopping step n, such oscillation disappears.

III. FLOQUET TOPOLOGICAL INSULATOR AND EDGE MODES INSIDE SINGLE CAVITY

For given time-periodic system with $H(t) = H(t+T)$, the quasienergy-state can be written as

$$\psi(r,t) = e^{-i\epsilon_q t}\phi(r,t) \tag{S6}$$

where ϵ_q is the quasienergy and $\phi(r,t) = \phi(r,t+T)$ are periodic functions, which are also named as Floquet modes [s38]. These modes satisfy

$$H_F(t)\phi_q(t) = \epsilon_q\phi_q(t) \tag{S7}$$

and

$$H_F(t) = H(t) - i\partial_t. \tag{S8}$$

Since different Floquet modes are physically equivalent when their quasienergies differ by $m\Omega$, it is therefore convenient to consider the first Floquet zone with $\epsilon \in (-\Omega/2, \Omega/2]$. The quasienergies and Floquet modes can be solved in the composite Floquet space $T \otimes R$ where R represents the usual Hilbert space and T is spanned by the periodic functions $\langle t|m\rangle = e^{im\Omega T}$. The index m describes the number of phonons involved in the interaction and defines the subspace named as m-th Floquet replica. Therefore in Floquet space, the periodic driven term induce an effective coupling between different Floquet replicas. The corresponding time-independent Floquet Hamiltonian in Floquet space $T \otimes R$ can be written as

$$\mathbb{H}_F = \hat{F}_m \otimes \hat{H}^{(m)} + \Omega\hat{F}_z \otimes I_R, \tag{S9}$$

where I_R means the identity operator in usual Hilbert space, $H(t) = \sum_m \hat{H}^{(m)}e^{im\Omega t}$, $(F_m)_{i,j} = \delta_{j,i+m}$, and $(F_z)_{m,n} = m\Omega\delta_{m,n}$. Using this formalism, the wave function in usual Hilbert space $|\psi\rangle = \sum_{m,j} c_{m,j}(t)\exp(im\Omega t)|j\rangle$ can be rewritten as $|\psi^F\rangle = \sum_{m,j} c_{m,j}(t)|m,j\rangle$, which satisfies the so-called Floquet Schrödinger equation

$$\frac{d|\psi^F\rangle}{dt} = -i\mathbb{H}_F|\psi^F\rangle - \frac{\gamma}{2}|\psi^F\rangle \tag{S10}$$

by taking into account the dissipation effect. This leads to the following evolution equations for each coefficient as

$$\frac{dc_{m,j}(t)}{dt} = -i[\mathbb{H}_F]_{mj,m'j'}c_{m',j'}(t) - \frac{\gamma_j}{2}c_{m,j}(t). \tag{S11}$$

The formal solution in frequency domain can be written as

$$c_{m,j}(\omega) = \frac{-1}{\sqrt{2\pi}}\langle m,j|\frac{1}{\omega + i\frac{\Gamma^F}{2} - \mathbb{H}_F}|\psi^F(0)\rangle \tag{S12}$$

with $|\psi^F(0)\rangle$ representing the initial state vector and $\Gamma^F = F_0 \otimes \Gamma$ the decay matrix in Floquet space. Mathematically, if we sum over all intermediate state $|m,j\rangle$ together with all possible initial vector $|\psi^F(0)\rangle$, we obtain the following total output spectrum as

$$T(\omega) = \sum_{\psi^F(0)}\sum_{m,j}|c_{m,j}(\omega)|^2$$

Fig. s6 shows the quasienergy spectra as a function of driven frequency Ω. We note that although the original static Hamiltonian is topological trivial for given parameters, a topological transition occurs when different replicas start to overlap with each other. In addition, the interaction of different Floquet replicas usually leads to the appearance of new gaps at $m\Omega/2$ with $m \in Z$ when lowering Ω.

To show how $T(\omega)$ can be distilled from the outputs of cavity modes, we rewrite the wavefunction in the usual Hilbert space as $|\psi\rangle = \sum_j d_j(t)|j\rangle$ with $d_j(t) = \sum_m c_{m,j}(t)\exp(im\Omega t)$. Since $c_{m,j}(t)$ changes much slowly during a single time period, the spectrum

$c_{m,j}(\omega)$ will mainly distributes within the regime $\omega \in (-\Omega/2, \Omega/2)$. Therefore, for given frequency ω, we can approximate $d_j(\omega) \simeq c_{M,j}(\omega - M\Omega)$ with $M = [\omega/\Omega]$ the integer closest to ω/Ω. Finally, we have

$$\begin{aligned} T(\omega) &= \sum_{\vec{\psi}(0)} \sum_{m,j} c^*_{m,j}(\omega) c_{m,j}(\omega) \\ &= \sum_{\vec{\psi}(0)} \sum_{m,j} d^*_j(\omega + m\Omega) d_j(\omega + m\Omega). \end{aligned} \quad \text{(S13)}$$

By monitoring the dynamics of different modes inside the cavity, we can obtain the output spectrum for $\omega \in (-\Omega/2, \Omega/2)$. In addition, when ω is resonant with Floquet modes, it will produce a peak in the spectrum. This provides an effective method to detect various Floquet gaps and edge modes in our system.

One of the particular properties of periodic driven system is presence of Floquet topological transition and mid-gapped edge modes even when their static Hamiltonian is topologically trivial. These features can be manifested by detecting the output spectrum $T(\omega)$ as outlined above. Compared with its static counterpart, Floquet topological system have two different kind of topological edge modes at $\epsilon = 0$ and $\Omega/2$. The presence of finite gap around $\epsilon = 0$ and $\Omega/2$ also enable us to detect Floquet topological phase transitions by observing the output spectrum due to the changes of edge modes. Specifically, when $\epsilon = 0$ or $\Omega/2$, mid-gapped edge modes contributes mostly to the summation in S13, while all contributions from other Floquet modes are greatly reduced due to the presence of finite gaps. The amplitude of $T(\omega)$ is approximately proportional to the total number of edge modes, which can be viewed as a direct evidence of Floquet topological phase transitions.

Floquet topological system usual exhibits distinct topological features compared with their static ones. The presence of different edge modes indicates that we need new topological invariants. The single-particle Bloch Hamiltonian reads

$$H(t,k) = [B_x(k) + \lambda \cos(\Omega t)]\sigma_x + B_y(k)\sigma_y. \quad \text{(S14)}$$

Since the system possesses chiral symmetry as $\sigma_z H(t,k)\sigma_z = -H(-t,k)$, the topological invariants associated with the number of end states v_0 and v_+ at $\epsilon = 0$ and $\Omega/2$ can be obtained from their time evolution operator defined as [s39, 40]

$$F(k) = \mathbb{T} \exp[-i \int_0^{T/2} H(t,k)] \quad \text{(S15)}$$

with $\mathbb{T}$ the time-ordering operator. Thanks to the chiral symmetry, the evolution of the second part of the cycle can be written as

$$\sigma_z F(k) \sigma_z = \mathbb{T} \exp[-i \int_{T/2}^{T} H(t,k)] \quad \text{(S16)}$$

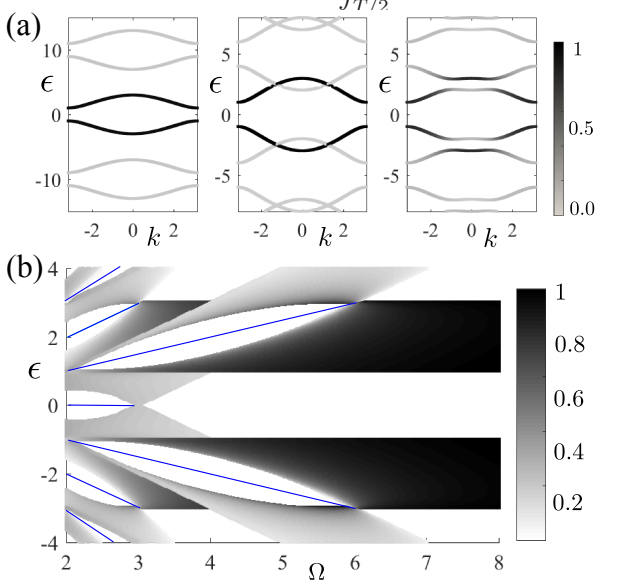

FIG. s6: (Color online). Floquet band structures ((a)) and spectrum (b) along with driven frequency Ω for a topologically trivial static Hamiltonian with $[J_0, J_1, \lambda] = [2, 1, 1.6]$. The corresponding parameters in the three panels of (a) are $(\Omega, \lambda) = (10, 1.6)$, $(\Omega, \lambda) = (5, 0)$, and $(\Omega, \lambda) = (5, 1.6)$ respectively (from left to right). The mid-gapped solid lines in (b) indicate the presence of edge states in finite system. The color bar indicates the weight of bulk states on the $m = 0$ Floquet subspace.

If we express $F(k)$ in the canonical form as

$$F(k) = \begin{pmatrix} a(k) & b(k) \\ c(k) & d(k) \end{pmatrix}, \quad \text{(S17)}$$

the winding number of blocks $b(k)$ and $d(k)$ gives the number of edge states at quasienergy $\epsilon = 0$ and $\Omega/2$ respectively

$$\begin{aligned} v_0 &= \frac{1}{2\pi i} \int_{-\pi}^{\pi} dk \frac{d}{dk} \ln \det b(k), \\ v_+ &= \frac{1}{2\pi i} \int_{-\pi}^{\pi} dk \frac{d}{dk} \ln \det d(k). \end{aligned}$$

We note that the above invariants are well defined only when the gap at $\epsilon = 0$ and $\Omega/2$ are not close. When the gaps are closed, $b(k)$ or $d(k)$ may has an eigenvalues of zero, which invalids the above definition.

[s1] C. Nayak, S. H. Simon, A. Stern, M. Freedman, and S. D. Sarma, Reviews of Modern Physics **80**, 1083 (2008).

[s2] M. Z. Hasan and C. L. Kane, Reviews of Modern Physics **82**, 3045 (2010).
[s3] X.-L. Qi and S.-C. Zhang, Reviews of Modern Physics **83**, 1057 (2011).
[s4] F. Haldane and S. Raghu, Phys. Rev. lett. **100**, 013904 (2008).
[s5] S. Raghu and F. Haldane, Phys. Rev. A **78**, 033834 (2008).
[s6] J. D. Joannopoulos, S. G. Johnson, J. N. Winn, and R. D. Meade, *Photonic crystals: molding the flow of light* (Princeton university press, 2011).
[s7] Z. Wang, Y. Chong, J. D. Joannopoulos, and M. Soljačić, Phys. Rev.Lett. **100**, 013905 (2008).
[s8] Z. Wang, Y. Chong, J. Joannopoulos, and M. Soljačić, Nature **461**, 772 (2009).
[s9] M. Hafezi, E. A. Demler, M. D. Lukin, and J. M. Taylor, Nature Physics **7**, 907 (2011).
[s10] K. Fang, Z. Yu, and S. Fan, Nature Photonics **6**, 782 (2012).
[s11] A. B. Khanikaev, S. H. Mousavi, W.-K. Tse, M. Kargarian, A. H. MacDonald, and G. Shvets, Nature Materials **12**, 233 (2013).
[s12] L. Lu, L. Fu, J. D. Joannopoulos, and M. Soljačić, Nature Photonics **7**, 294 (2013).
[s13] Y. E. Kraus, Y. Lahini, Z. Ringel, M. Verbin, and O. Zilberberg, Phys. Rev. Lett. **109**, 106402 (2012).
[s14] M. C. Rechtsman, J. M. Zeuner, Y. Plotnik, Y. Lumer, D. Podolsky, F. Dreisow, S. Nolte, M. Segev, and A. Szameit, Nature **496**, 196 (2013).
[s15] M. Hafezi, S. Mittal, J. Fan, A. Migdall, and J. Taylor, Nature Photonics **7**, 1001 (2013).
[s16] L. Lu, J. D. Joannopoulos, and M. Soljačić, Nature Photonics **8**, 821 (2014).
[s17] W.-J. Chen, S.-J. Jiang, X.-D. Chen, B. Zhu, L. Zhou, J.-W. Dong, and C. Chan, Nature Communications **5**, 5782 (2014).
[s18] L. Lu, Z. Wang, D. Ye, L. Ran, L. Fu, J. D. Joannopoulos, and M. Soljačić, Science **349**, 622 (2015).
[s19] N. Schine, A. Ryou, A. Gromov, A. Sommer, and J. Simon, Nature **534**, 671 (2016).
[s20] G. Liang and Y. Chong, Phys. Rev. Lett. **110**, 203904 (2013).
[s21] R. Umucalılar and I. Carusotto, Phys. Rev. A **84**, 043804 (2011).
[s22] S. A. Skirlo, L. Lu, and M. Soljačić, Phys. Rev. Lett. **113**, 113904 (2014).
[s23] S. Mittal, J. Fan, S. Faez, A. Migdall, J. Taylor, and M. Hafezi, Phys. Rev. Lett. **113**, 087403 (2014).
[s24] W. Hu, J. C. Pillay, K. Wu, M. Pasek, P. P. Shum, and Y. D. Chong, Phys. Rev. X **5**, 011012 (2015).
[s25] W. Gao, M. Lawrence, B. Yang, F. Liu, F. Fang, B. Béri, J. Li, and S. Zhang, Phys. Rev. Lett. **114**, 037402 (2015).
[s26] M. Hafezi, Phys. Rev. Lett. **112**, 210405 (2014).
[s27] A. Celi, P. Massignan, J. Ruseckas, N. Goldman, I. B. Spielman, G. Juzeliūnas, and M. Lewenstein, Phys. Rev. Lett. **112**, 043001 (2014).
[s28] H. M. Price, O. Zilberberg, T. Ozawa, I. Carusotto, and N. Goldman, Phys. Rev. Lett. **115**, 195303 (2015).
[s29] T.-S. Zeng, C. Wang, and H. Zhai, Phys. Rev. Lett. **115**, 095302 (2015).
[s30] F. Mei, J.-B. You, D.-W. Zhang, X. C. Yang, R. Fazio, S.-L. Zhu, and L. C. Kwek, Phys. Rev. A **90**, 063638 (2014).
[s31] A. M. Yao and M. J. Padgett, Advances in Optics and Photonics **3**, 161 (2011).
[s32] H. M. Price, T. Ozawa, and N. Goldman, arXiv preprint arXiv:1605.09310 (2016).
[s33] X.-W. Luo, X. Zhou, C.-F. Li, J.-S. Xu, G.-C. Guo, and Z.-W. Zhou, Nature Communications **6**, 7704 (2015).
[s34] See Supplimental Material for explicit introduction of degenerated cavity, the reduction of hopping amplitudes due to the pinhole, and calculation details about Floquet topological system, which includes Ref. [s33, 35–40].
[s35] J. Arnaud, Applied optics **8**, 189 (1969).
[s36] S. A. Collins, JOSA **60**, 1168 (1970).
[s37] N. Hodgson and H. Weber, *Laser Resonators and Beam Propagation: Fundamentals, Advanced Concepts, Applications*, Vol. 108 (Springer, 2005).
[s38] T. Levante, M. Baldus, B. Meier, and R. Ernst, Molecular Physics **86**, 1195 (1995).
[s39] J. Asbóth, B. Tarasinski, and P. Delplace, Phys. Rev. B **90**, 125143 (2014).
[s40] V. Dal Lago, M. Atala, and L. F. Torres, Phys. Rev. A **92**, 023624 (2015).
[s41] T. Oka and H. Aoki, Phys. Rev. B **79**, 081406 (2009).
[s42] T. Kitagawa, E. Berg, M. Rudner, and E. Demler, Phys. Rev. B **82**, 235114 (2010).
[s43] N. H. Lindner, G. Refael, and V. Galitski, Nature Physics **7**, 490 (2011).
[s44] J. Cayssol, B. Dóra, F. Simon, and R. Moessner, physica status solidi (RRL)-Rapid Research Letters **7**, 101 (2013).
[s45] A. Gómez-León and G. Platero, Phys. Rev. Lett. **110**, 200403 (2013).
[s46] M. Pasek and Y. Chong, Phys. Rev. B **89**, 075113 (2014).
[s47] D. Leykam, M. C. Rechtsman, and Y. D. Chong, Phys. Rev. Lett. **117**, 013902 (2016).
[s48] W.-P. Su, J. Schrieffer, and A. Heeger, Phys. Rev. B **22**, 2099 (1980).
[s49] D. F. Walls and G. J. Milburn, *Quantum optics* (Springer Science & Business Media, 2007).
[s50] P. Harper, Proceedings of the Physical Society. Section A **68**, 874 (1955).
[s51] S. Aubry and G. Andr, Israel Phys. Soc. **3**, 133 (1980).
[s52] A. J. Kollár, A. T. Papageorge, V. D. Vaidya, Y. Guo, J. Keeling, and B. L. Lev, arXiv preprint arXiv:1606.04127 (2016).
[s53] H. Schmidt and A. Imamoglu, Optics letters **21**, 1936 (1996).
[s54] A. Imamolu, H. Schmidt, G. Woods, and M. Deutsch, Phys. Rev. Lett. **79**, 1467 (1997).
[s55] S. Harris and Y. Yamamoto, Phys. Rev. Lett. **81**, 3611 (1998).